Theor Chem Acc (2015) 134:120
DOI 10.1007/s00214-015-1726-3

REGULAR ARTICLE

Dissecting the bond-formation process of d^{10}-metal–ethene complexes with multireference approaches

Yilin Zhao[1] · Katharina Boguslawski[1,2] · Paweł Tecmer[1] · Corinne Duperrouzel[1] · Gergely Barcza[3] · Örs Legeza[3] · Paul W. Ayers[1]

Received: 22 May 2015 / Accepted: 30 August 2015 / Published online: 23 September 2015

Abstract The bonding mechanism of ethene to a nickel or palladium center is studied by the density matrix renormalization group algorithm, the complete active space self-consistent field method, coupled cluster theory, and density functional theory. Specifically, we focus on the interaction between the metal atom and bis-ethene ligands in perpendicular and parallel orientations. The bonding situation in these structural isomers is further scrutinized using energy decomposition analysis and quantum information theory. Our study highlights the fact that when two ethene ligands are oriented perpendicular to each other, the complex is stabilized by the metal-to-ligand double-back-bonding mechanism. Moreover, we demonstrate that nickel–ethene complexes feature a stronger and more covalent interaction between the ligands and the metal center than palladium–ethene compounds with similar coordination spheres.

Keywords d^{10}-Transition metals · DMRG · CASSCF · Orbital entanglement · Energy decomposition analysis · Back-bonding · π-Donation

1 Introduction

d^{10}-Transition metals like Ni, Pd, and Pt are very versatile metals used in batteries, alloys, and catalysts. In particular, in organometallic chemistry, they play an important role in catalytic processes like coupling reactions [1–4] and cycloaddition reactions [5, 6]. Unsaturated organic compounds like olefins can easily form organometallic complexes with d^{10}-transition metals by metal–olefin bonding. It is commonly believed that the so-called metal–olefin bonds are formed by the process of back-donation.

The Dewar–Chatt–Duncanson model [7, 8] is widely used to explain the back-donation process between metals and olefins. Metal d-orbitals overlap with olefin π^*-orbitals, allowing electron transfer from metal d-orbitals to ligand π^*-orbitals. The electron transfer process from bonding metal to antibonding ligand orbitals reduces the bond order of the ligand π-bonds. This destabilizes the carbon–carbon double bond and lowers the energy barrier to bond cleavage [9–15] (Fig. 1).

Recently, we elucidated the nickel–ethene reaction pathway and the crucial role of metal-to-ligand back-donation in the metal–olefin bond-formation process [16]. Our study reveals the presence of a transition state along the nickel–ethene reaction pathway. This peculiar feature in the metal–olefin bond-formation process motivates this study of other d^{10}-transition metal complexes containing a nickel

Electronic supplementary material The online version of this article (doi:10.1007/s00214-015-1726-3) contains supplementary material, which is available to authorized users.

✉ Katharina Boguslawski
katharina.boguslawski@gmail.com

✉ Paweł Tecmer
ptecmer@gmail.com

Örs Legeza
legeza.ors@wigner.mta.hu

[1] Department of Chemistry and Chemical Biology, McMaster University, 1280 Main Street West, Hamilton L8S 4M1, Canada

[2] Present Address: Faculty of Physics, Astronomy and Informatics, Institute of Physics, Nicolaus Copernicus University, Grudziądzka 5, 87-100 Toruń, Poland

[3] Strongly Correlated Systems "Lendület" Research Group, Wigner Research Centre for Physics, Budapest 1525, Hungary

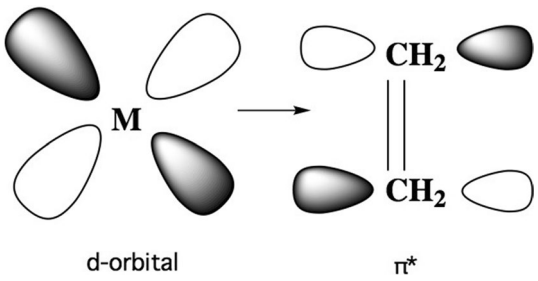

Fig. 1 Schematic representation of the back-donation process. *M* refers to either palladium or nickel

and palladium center and their reactions with small olefin ligands [9, 17]. The bond-formation process of d^{10}-transition metals and olefins can be dissected using the energy decomposition analysis (EDA) and an orbital entanglement analysis, which allows us to identify the most important orbital interaction along the reaction coordinate.

In the EDA developed by Morokuma [18, 19] and Ziegler and Rauk [20–23], the quantum system is divided into disjoint fragments according to the interaction of interest. In this work, the interaction energy between ligand(s) and the metal center, ΔE_{int}, is decomposed into three main components,

$$\Delta E_{\text{int}} = \Delta V_{\text{elstat}} + \Delta E_{\text{Pauli}} + \Delta E_{\text{oi}}, \tag{1}$$

where ΔV_{elstat} denotes the electrostatic interaction energy, ΔE_{Pauli} is the repulsive Pauli interaction, and ΔE_{oi} denotes the orbital interaction between the fragments. The EDA has proven to be a very powerful tool for analyzing chemical bonds and orbital interactions in many complex chemical systems, including transition metal complexes [24–26].

Quantum information theory allows us to quantify the interaction and correlation of orbitals and orbital pairs [27–32]. The entanglement between one orbital and the orbital bath is measured by the von Neumann entropy of the reduced density matrix of the orbital of interest, here referred to as one-orbital reduced density matrix. The eigenvalues of the one-orbital reduced density matrix ω_α are used to calculate the single-orbital entropy [33],

$$s(1)_i = -\sum_\alpha \omega_{\alpha,i} \ln \omega_{\alpha,i}. \tag{2}$$

We refer the interested reader to Refs. [27, 28, 32, 34] for more details on how to calculate orbital reduced density matrices. Similarly, the entanglement of two orbitals with the orbital bath is quantified by the two-orbital entropy $s(2)_{i,j}$,

$$s(2)_{i,j} = -\sum_\alpha \omega_{\alpha,i,j} \ln \omega_{\alpha,i,j}, \tag{3}$$

where $\omega_{\alpha,i,j}$ are the eigenvalues of the two-orbital reduced density matrix.

The correlation between orbital pair i and j can be measured by the orbital-pair mutual information [29, 33, 35],

$$I_{i|j} = \frac{1}{2}(s(2)_{i,j} - s(1)_i - s(1)_j)(1 - \delta_{ij}), \tag{4}$$

where δ_{ij} is the Kronecker delta.

Both $s(1)_i$ and $I_{i|j}$ quantify orbital interactions and can be used to identify different types of electron correlation effects [31, 36, 37], dissect chemical bonding [30, 32, 38–40], and locate transition state structures in molecular systems [16, 41, 42].

In this work, we investigate the bonding situation in nickel–ethene and palladium–ethene compounds using wavefunction approaches such as the complete active space self-consistent field approach, the density matrix renormalization group algorithm, and coupled cluster theory. In particular, we investigate the potential energy surfaces resulting from the interaction of the ethene molecule(s) approaching the palladium center in three structural rearrangements $Pd(C_2H_4)$, $Pd(C_2H_4)_2^{(\parallel)}$, and $Pd(C_2H_4)_2^{(\perp)}$, where $\parallel$ indicates that the ethene ligands are aligned in parallel, while $\perp$ indicates a perpendicular orientation of the ethene ligands (see Fig. 2). In the case of nickel–ethene, we augment our previous analysis of the $Ni(C_2H_4)$ reaction pathway with the symmetric bond-formation process of $Ni(C_2H_4)_2^{(\parallel)}$ and $Ni(C_2H_4)_2^{(\perp)}$. Furthermore, the bonding interaction between the transition metals (Ni, Pd) and the ethene ligand(s) is analyzed in terms of the energy

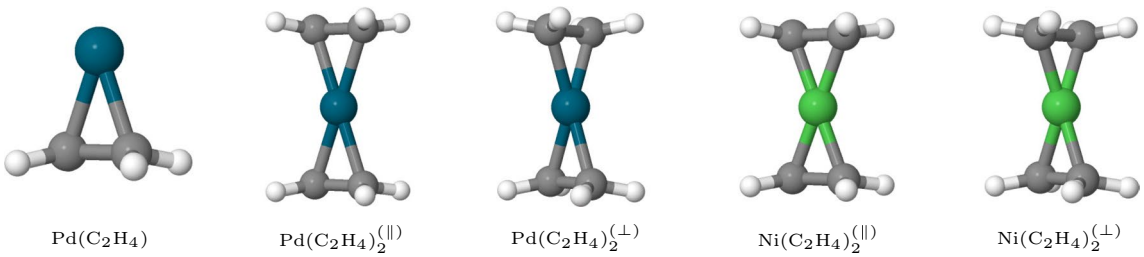

Fig. 2 Equilibrium structures of nickel–ethene and palladium–ethene complexes optimized by BP86. The $\parallel$ symbol indicates that both ethene ligands are aligned parallel to each other, while the $\perp$ symbol is used to label the perpendicular arrangement of the ethene ligands

decomposition analysis as implemented in ADF [20, 23] and an orbital entanglement analysis.

This paper is organized as follows. Section 2 contains the computational details. In Sect. 3, the bond-formation process of different nickel–ethene and palladium–ethene complexes is dissected using the EDA and orbital entanglement analysis. Finally, we conclude in Sect. 4.

2 Computational details

2.1 Geometry optimization

The structures of all metal–ethene complexes are optimized by scanning the nickel–carbon bond from 1.80 Å to 2.80 Å and the palladium–carbon bond from 2.05 Å to 4.05 Å (constrained geometry optimization). In case of $Ni(C_2H_4)_2$, an additional reaction pathway was investigated where one ethene molecule approached the $Ni(C_2H_4)$ fragment. In this asymmetric bond-formation process, all nickel–carbon distances were constrained, while all hydrogen atoms were allowed to freely relax. All calculations were performed with the ADF2013 software package [43–45]. Scalar relativistic effects were included using the ZORA Hamiltonian [46–48]. In all calculations, a DZP [49] basis set and the BP86 [50, 51] exchange–correlation functional were used.

2.2 CASSCF

Complete active space self-consistent field (CASSCF) [52–54] calculations for nickel–ethene were performed in the DALTON2013 [55] software package, while the MOLPRO2012 [56, 57] software suite was used for palladium–ethene. A TZP ANO-RCC basis set was employed in all CASSCF calculations with the following contraction schemes: $H : (8s4p3d1f) \rightarrow [6s4p3d1f]$ [58], $C : (8s7p4d3f2g) \rightarrow [4s3p2d1f]$ [59], $Ni : (10s9p8d6f4g2h) \rightarrow [6s5p3d2f1g]$ [60], and $Pd : (21s18p13d6f4g2h) \rightarrow [10s9p9d6f4g2h]$ [60]. Scalar relativistic effects were included by the second-order Douglas–Kroll–Hess Hamiltonian [61, 62]. The CASSCF orbitals were visualized using the Jmol14.2.7 [63] visualization software.

For $Ni(C_2H_4)_2^{(\perp)}$ $(n = 3)$ as well as $Pd(C_2H_4)_2^{(\perp)}$ and $Pd(C_2H_4)_2^{(\parallel)}$ $(n = 4)$, we correlated 14 electrons in 14 orbitals, including the nd_{xy}, nd_{xz}, nd_{yz}, nd_{z^2}, $nd_{x^2-y^2}$, and $(n+1)d_{xy}$, $(n+1)d_{xz}$, $(n+1)d_{yz}$, $(n+1)d_{z^2}$, $(n+1)d_{x^2-y^2}$ orbitals from the d^{10}-transition metals and both π and π^* orbitals from the ethene ligands. For $Ni(C_2H_4)_2^{(\parallel)}$, the Ni $4d_{xy}$-orbital was excluded resulting in CAS(14,13)SCF calculations.

For the $Pd(C_2H_4)$ complex, we performed CAS(12,12)SCF and CAS(14,14)SCF calculations. The CAS(12,12)SCF active space contains the metal 4*d*/5*d* and the ethene π- and π^*-orbitals. To evaluate the contribution of the σ and σ^* orbitals, the CAS(12,12)SCF active space was extended to 14 electrons correlated in 14 orbitals in our CAS(14,14)SCF calculations. The resulting CASSCF orbitals along the potential energy surfaces are presented in Figures S1–S18 of the Supporting Information.

C_{2v} symmetry was imposed for $Pd(C_2H_4)$, D_{2h} symmetry for $Ni(C_2H_4)_2^{(\parallel)}$ and $Pd(C_2H_4)_2^{(\parallel)}$, and D_2 symmetry for $Ni(C_2H_4)_2^{(\perp)}$ and $Pd(C_2H_4)_2^{(\perp)}$.

2.3 UCCSD and UCCSD(T)

The Unrestricted Coupled Cluster Singles Doubles (UCCSD) and UCCSD and perturbative Triples (UCCSD(T)) [64] calculations were performed with the MOLPRO2012 [56, 57] program. The core orbitals were kept frozen, while all virtual orbitals were correlated. The same basis sets, point group symmetries, and relativistic Hamiltonian were used as in our CASSCF calculations. The UCCSD(T) energies are collected in Tables S1–S5 of the Supporting Information.

2.4 EDA

The energy decomposition analysis calculations were performed for the nickel–ethene and palladium–ethene complexes at equilibrium distance using the ADF2013 [43–45] software package. Specifically, the supramolecule was divided into one fragment containing the metal center and a second fragment containing the ethene ligand for monoligated complexes, while a third fragment comprising the second ethene ligand was added for the biligated metal compounds.

2.5 DMRG

The BUDAPEST DMRG [65] program was used to perform the density matrix renormalization group (DMRG) [66–68] calculations. As orbital basis, the natural orbitals obtained from the largest CASSCF calculations as described in the previous subsection were used. For the biligated nickel complexes, the active spaces were extended by including additional occupied and virtual natural orbitals. Specifically, 10 additional occupied orbitals ($2 \times A_g$, $2 \times B_{3u}$, $1 \times B_{2u}$, $1 \times B_{1g}$, $1 \times B_{1u}$, $1 \times B_{2g}$, $1 \times B_{3g}$ and $1 \times A_u$) and 10 virtual orbitals ($2 \times A_g$, $1 \times B_{3u}$, $1 \times B_{2u}$, $1 \times B_{1g}$, $1 \times B_{1u}$, $1 \times B_{2g}$, $2 \times B_{3g}$ and $1 \times A_u$) were added for $Ni(C_2H_4)_2^{(\parallel)}$, increasing it to 34 electrons correlated in 33 orbitals (DMRG(34,33)). For $Ni(C_2H_4)_2^{(\perp)}$, 11 occupied ($3 \times A$, $2 \times B_1$, $3 \times B_3$ and $3 \times B_2$) and 8 virtual orbitals ($3 \times A$, $1 \times B_1$, $2 \times B_3$ and $2 \times B_2$) were added, resulting in DMRG(36,33). The DMRG calculations for Pd complexes were carried out with the same

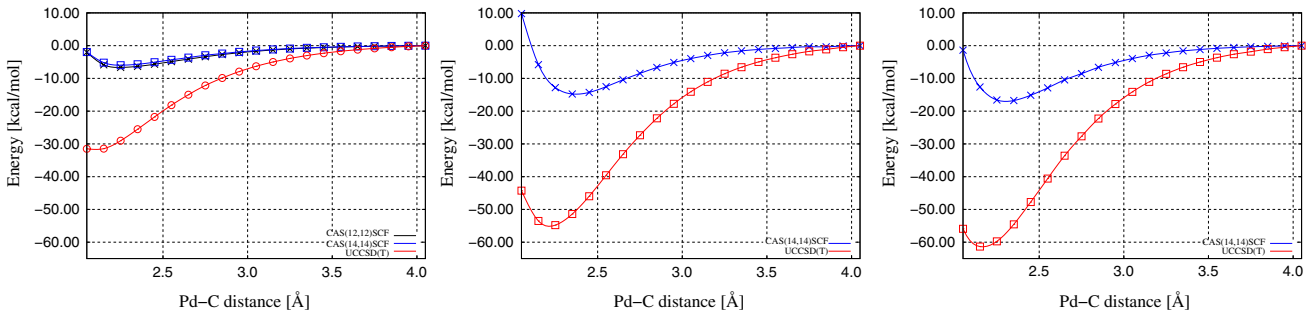

(a) $Pd(C_2H_4)$ **(b)** $Pd(C_2H_4)_2^{(\parallel)}$ **(c)** $Pd(C_2H_4)_2^{(\perp)}$

Fig. 3 Potential energy surfaces for the palladium–ethene reaction pathway in different structural rearrangements. In the case of two ethene molecules, the potential energy surfaces result from the symmetric dissociation of the ethene ligands from the metal center. The last point of the reaction coordinate is adjusted to zero

Table 1 Bonding energies for metal–ethene complexes in kcal/mol for CASSCF and CCSD(T)

Molecular	CASSCF	UCCSD(T)
$Ni(C_2H_4)_2^{(\parallel)}$	>39.0	n/a
$Ni(C_2H_4)_2^{(\perp)}$	>39.0	n/a
$Pd(C_2H_4)$	6.6	29.0
$Pd(C_2H_4)_2^{(\parallel)}$	14.8	51.4
$Pd(C_2H_4)_2^{(\perp)}$	16.8	54.5

active spaces as in CASSCF. Furthermore, we made sure that the active spaces contained similar orbitals along the reaction coordinate, i.e., molecular orbitals with similar atomic contributions.

To enhance convergence, we optimized the orbital ordering [30]. The initial guess was generated using the dynamically extended-active-space procedure (DEAS) [33]. In all DMRG calculations, the Davidson diagonalization threshold was set to 10^{-6} for the nickel complexes, and 10^{-7} for the palladium compounds. The minimum number of block states, m, was set to 64 (in the preoptimization), while the maximum number was set to 1024. The convergence of DMRG with respect to m is summarized in Tables S1–S5 of the Supporting Information.

The orbital entanglement and correlations diagrams were determined from the DMRG wavefunctions as described in Ref. [32].

3 Numerical results

3.1 Geometries and potential energy surfaces

The DFT-optimized geometries along the metal–ethene dissociation pathway are summarized in the Supporting Information. Figure 2 shows the equilibrium structures of all investigated metal–ethene compounds. For all optimized structures, the hydrogen atoms of the ethene molecule are slightly bent outside the molecular (C–C–H) plane of the uncoordinated ethene.

The potential energy surfaces for the palladium–ethene dissociation process are displayed in Fig. 3, while Table 1 summarizes the bonding energy, i.e., the energy difference between the equilibrium structure and the dissociation limit. In general, $Pd(C_2H_4)_2^{(\perp)}$ has the largest energy to association in both CASSCF and UCCSD(T) calculations. The missing dynamic electron correlation energy in CASSCF leads to shallower potential energy well depths compared to the CC results. In contrast to the monoligated nickel–ethene complex [16], all investigated quantum chemistry methods predict no barrier to association along the palladium–ethene reaction coordinate.

Figure 4 shows the potential energy surfaces for the symmetric nickel–ethene dissociation pathway predicted by CASSCF, DMRG, and UCCSD. We were unable to converge the constrained geometry optimization for Ni–C distances larger than 2.80 Å. Thus, only estimated potential well depths and bonding energies of $Ni(C_2H_4)_2^{(\parallel)}$ and $Ni(C_2H_4)_2^{(\perp)}$ are provided. Furthermore, we encountered convergence difficulties in our UCCSD calculations for stretched distances of $Ni(C_2H_4)_2$. Therefore, it remains unclear whether the symmetric dissociation of $Ni(C_2H_4)_2$ features a transition state as found for the monoligated nickel–ethene complex.

As shown in Table 1, the lower bound for the bonding energy is considerably larger in nickel–ethene than in palladium–ethene complexes, suggesting a stronger bonding interaction between the nickel center and the ethene ligands in terms of π-donation and metal-to-ligand back-bonding.

In general, CC calculations predict shorter metal–ethene bond lengths than found in CASSCF, which can be attributed to the missing dynamic electron correlation effects in

the latter. Specifically, the CASSCF Pd–C equilibrium distance in $Pd(C_2H_4)$ is approximately 2.25 Å, which reduces to 2.10 Å in UCCSD(T). For $Pd(C_2H_4)_2^{(\parallel)}$, the equilibrium bond length decreases from 2.35 Å in CASSCF to 2.25 Å in UCCSD(T), while the equilibrium bond lengths are slightly shorter for $Pd(C_2H_4)_2^{(\perp)}$: 2.35 Å in CASSCF and 2.15 Å in UCCSD(T).

3.2 Elucidating the metal-to-ligand back-donation

3.2.1 Energy decomposition analysis

The EDA results at the equilibrium distance for all metal–ethene complexes are summarized in Table 2. The total interaction energy (see Table 2) is defined as the sum of ΔE_{Pauli}, ΔV_{elstat}, and ΔE_{oi} and quantifies the interaction between the fragments.

All investigated nickel–ethene complexes have a considerably larger total interaction energy (in absolute value) than the corresponding palladium–ethene compounds with similar coordination sphere. Comparing ΔV_{elstat} with ΔE_{oi}, we observe that ΔV_{oi} constitutes the dominant contribution in nickel–ethene complexes, while ΔV_{elstat} dominates in palladium–ethene complexes. Since ΔV_{elstat} corresponds to the classic electrostatic interaction between fragments and ΔE_{oi} represents the interaction between orbitals on one fragment with the orbitals on the other fragment, a larger contribution of ΔV_{elstat} indicates more ionic interactions between the fragments, while a larger contribution of ΔE_{oi} suggests a stronger covalent nature of the interaction between the fragments. The different ratios between ΔV_{elstat} and ΔE_{oi} suggest that the nickel–ligand bond is more covalent, while the palladium–ligand bond is more ionic.

3.2.2 Orbital entanglement

An orbital entanglement analysis uses the single-orbital entropy $s(1)_i$ to measure orbital entanglement and the orbital-pair mutual information $I_{i|j}$ to quantify the correlation between orbital pairs. Both $s(1)_i$ and $I_{i|j}$ are represented using diagrams. Specifically, the strength of the orbital-pair mutual information is color-coded. Strongly correlated orbital pairs are connected by blue lines ($I_{i|j} \approx 10^{-1}$), moderately correlated orbitals by red lines ($I_{i|j} \approx 10^{-2}$), while weakly correlated orbitals are indicated by green lines ($I_{i|j} \approx 10^{-3}$), etc. As presented in Ref. [31], the strength of orbital entanglement and correlation can be associated with electron correlation effects [69, 70] (see Table 3). Since we are interested in bond-formation processes, our analysis will focus on orbitals and orbital pairs with moderately to strongly entangled orbitals, i.e., orbitals with $s(1)_i > 0.1$ and $I_{i|j} > 10^{-2}$.

Table 2 Energy decomposition analysis for nickel–ethene and palladium–ethene complexes

Molecule	r_e(Å)	ΔE_{Pauli} ($\frac{\text{kcal}}{\text{mol}}$)	ΔV_{elstat} ($\frac{\text{kcal}}{\text{mol}}$)	ΔE_{oi} ($\frac{\text{kcal}}{\text{mol}}$)	E_{int} ($\frac{\text{kcal}}{\text{mol}}$)
$Ni(C_2H_4)$	1.88	385.3	−220.1 (47 %)	−251.7 (53 %)	−86.6
$Ni(C_2H_4)_2^{(\parallel)}$	2.02	591.9	−313.4 (45 %)	−387.2 (55 %)	−108.6
$Ni(C_2H_4)_2^{(\perp)}$	2.02	595.3	−314.5 (43 %)	−411.2 (57 %)	−133.7
$Pd(C_2H_4)$	2.25	125.2	−109.4 (58 %)	−58.2 (42 %)	−42.4
$Pd(C_2H_4)_2^{(\parallel)}$	2.35	184.4	−165.9 (66 %)	−83.4 (34 %)	−64.9
$Pd(C_2H_4)_2^{(\perp)}$	2.35	184.7	−166.5 (65 %)	−89.6 (35 %)	−77.3

r_e is the equilibrium distance between the metal center and the carbon atom of the ethene molecule(s). ΔV_{elstat} is the electrostatic interaction energy, ΔE_{Pauli} is the repulsive Pauli interaction, and ΔE_{oi} refers to the orbital interaction between the fragments. $E_{\text{int}} = \Delta E_{\text{Pauli}} + \Delta V_{\text{elstat}} + \Delta E_{\text{oi}}$ is the total interaction energy

Orbital entanglement and correlation in palladium–ethene Figs. 5, 6, and 7 show the mutual information and single-orbital entropy for palladium–ethene complexes at different points of the reaction coordinate (see Fig. 3) along with the strongly entangled molecular orbitals.

For the monoligated $Pd(C_2H_4)$ in the dissociation limit (Fig. 5c), molecular orbitals centered on the metal atom (Pd 4*d*- and 5*d*-orbitals) and on the ethene fragment (π- and π^*-orbitals) are correlated. No significant orbital correlations can be observed between orbitals centered on different fragments. The most strongly correlated orbitals are the ethene π- and π^*-orbitals (nos. 3 and 9 in Fig. 5c). When the ethene molecule approaches the metal center (see Fig. 5b), the Pd d_{yz}-orbital (no. 8) and the ethene π^*-orbital (no. 9) become weakly correlated. This orbital correlation corresponds to the metal-to-ligand back-donation process. However, the most strongly correlated orbitals remain centered on the ethene ligand (π-π^*) and the metal atom (4*d*-5*d*), respectively. Around the equilibrium structure, the molecular orbitals involved in metal-to-ligand back-bonding (nos. 8 and 9 in Fig. 5a) become moderately correlated, while molecular orbitals involved in π-donation from the ethene π-orbitals to the Pd $4d_{z^2}$-orbital (nos. 2 and 3 in Fig. 5a) are only weakly correlated. The dominant orbital correlations remain between the ethene π- and π^*-orbitals and between Pd 4*d*- and 5*d*-orbitals.

A similar trend in the orbital correlation and entanglement diagrams can be observed for $Pd(C_2H_4)_2^{(\parallel)}$ (see

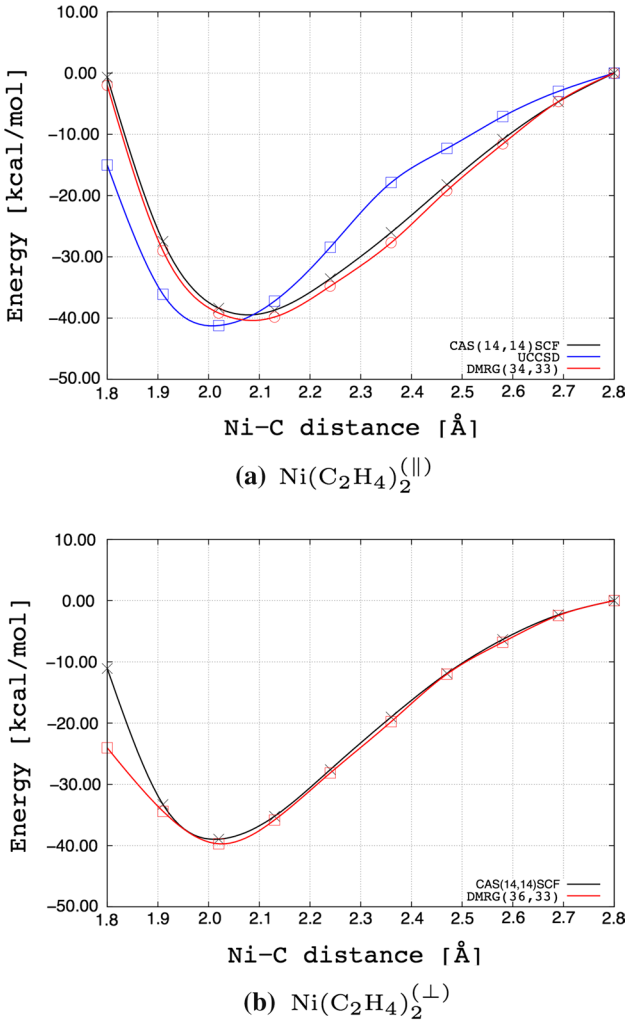

Fig. 4 Potential energy surfaces for the nickel–ethene reaction pathway in different structural rearrangements. The potential energy surfaces correspond to the symmetric dissociation of the ethene ligands from the metal center. The *last point* of the reaction coordinate is adjusted to zero

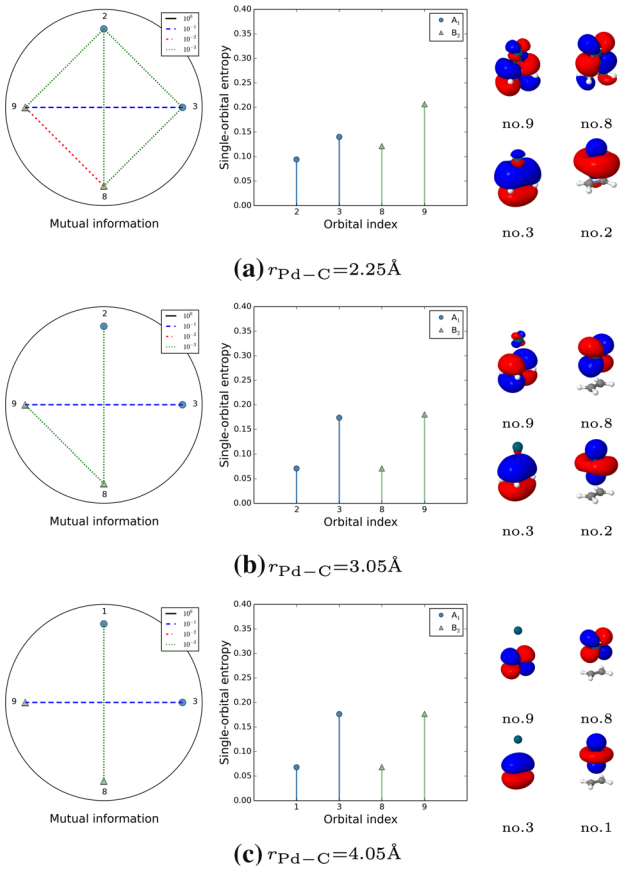

Fig. 5 Orbital-pair mutual information and single-orbital entropy for $Pd(C_2H_4)$ determined from DMRG(14,14) calculations. Only the strongly correlated/entangled orbitals are shown, i.e., $s(1)_i > 0.1$ and $I_{i|j} > 10^{-2}$

Table 3 Relation between the strength of orbital entanglement and correlation and electron correlation effects

Correlation effects	$s(1)_i$	$I_{i\|j}$
Nondynamic	>0.5	$\approx 10^{-1}$
Static	0.5–0.1	$\approx 10^{-2}$
Dynamic	<0.1	$\approx 10^{-3}$

Fig. 6). In the dissociation limit (Fig. 6c), orbital correlations remain distributed among the ethene π- and π^*-orbitals (nos. 3, 6, 9, and 13) as well as Pd 4*d*- and 5*d*-orbitals (nos. 1 and 12). When both ethene ligands approach the Pd center (see Fig. 6b), the Pd d_{yz}-orbital (no. 12) and the ligand $(\pi_1^* + \pi_2^*)$-orbital (no. 13) are weakly correlated. These orbitals are involved in the metal-to-ligand backbonding process. However, the dominant orbital correlations remain centered on the ligand orbitals and on the metal orbitals, respectively. Around the equilibrium structure, the changes in the correlation and entanglement patterns are more profound than for the monoligated palladium–ethene complex. While the Pd d_{yz}-orbital (no. 12) and the ligand $(\pi_1 + \pi_2)$-orbital (no. 13) are moderately correlated, the correlation strength between the ligand $(\pi_1^* + \pi_2^*)$-orbital and the remaining bonding and antibonding combinations of the π- and π^*-orbitals decreases. Similarly, the Pd d_{z^2}-orbital and the ligand $(\pi_1 + \pi_2)$-orbital are weakly entangled, suggesting a negligible contribution of π-donation in the bond-formation process of $Pd(C_2H_4)_2^{(\parallel)}$.

For $Pd(C_2H_4)_2^{(\perp)}$, the Pd *d*-orbitals and the ligand π- and π^*-orbitals remain uncorrelated in the dissociation limit and for stretched palladium–ethene distances (see Fig. 7b, c). In contrast to $Pd(C_2H_4)$ and $Pd(C_2H_4)_2^{(\parallel)}$, the correlation and entanglement diagrams drastically change around the equilibrium distance (see Fig. 7a). At this point, the Pd $4d_{yz}$-orbital (no. 9) and the ligand (π_1^*, π_2^*)-orbital

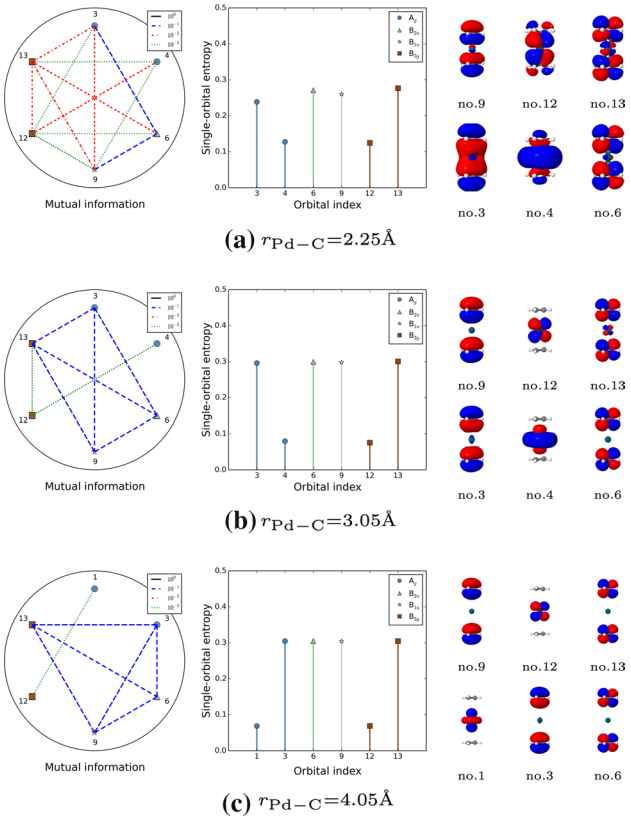

Fig. 6 Orbital-pair mutual information and single-orbital entropy for $Pd(C_2H_4)_2^{\parallel}$ determined from DMRG(14,14) calculations. Only the strongly correlated/entangled orbitals are shown, i.e., $s(1)_i > 0.1$ and $I_{i|j} > 10^{-2}$

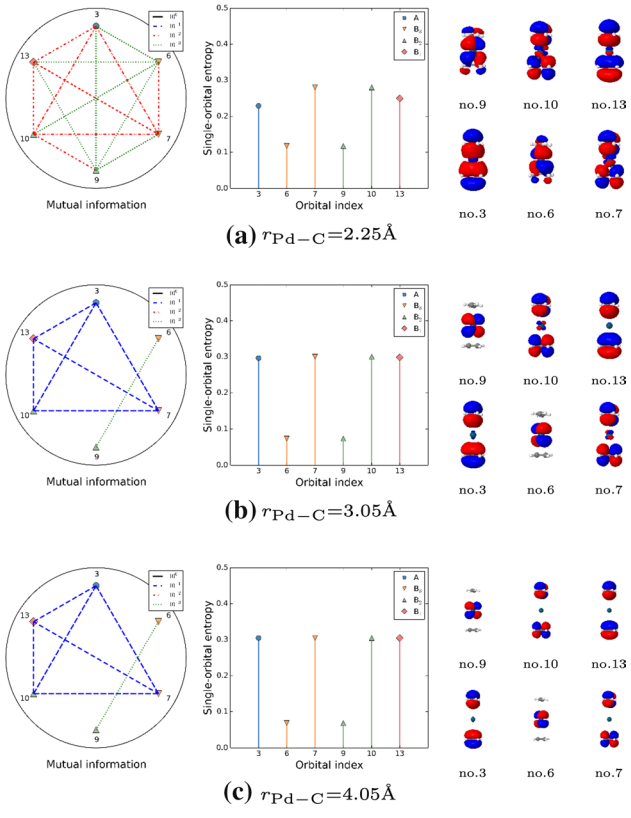

Fig. 7 Orbital-pair mutual information and single-orbital entropy for $Pd(C_2H_4)_2^{\perp}$ determined from DMRG(14,14) calculations. Only the strongly correlated/entangled orbitals are shown, i.e., $s(1)_i > 0.1$ and $I_{i|j} > 10^{-2}$

(no. 10) as well as the Pd $4d_{xz}$-orbital (no. 6) and the ligand (π_3^*, π_4^*)-orbital (no. 7) are moderately correlated. Furthermore, the correlation between the ligand π and π^*-orbitals (nos. 3, 7, 10, and 13) reduces, and all ligand orbitals are only moderately correlated compared to the ligand orbitals in $Pd(C_2H_4)$ and $Pd(C_2H_4)_2^{(\parallel)}$. These dominant correlations between metal and ligand orbitals suggest that the electronic structure of $Pd(C_2H_4)_2^{(\perp)}$ features two metal-to-ligand back-bonding interactions. This *double-back-bonding* mechanism may lead to an additional stabilization of the $Pd(C_2H_4)_2^{(\perp)}$ isomer compared to the $Pd(C_2H_4)_2^{(\parallel)}$ complex and elucidates the larger orbital interaction energy ΔE_{oi} of $Pd(C_2H_4)_2^{(\perp)}$ in the EDA.

Orbital entanglement and correlation in nickel–ethene The entanglement and correlation diagrams for $Ni(C_2H_4)_2^{(\parallel)}$ at different points along the reaction coordinate are shown in Fig. 8. In the dissociation limit, the leading orbital correlation is found between the Ni $3d_{z^2}$- and $4s$-orbitals (nos. 4 and 6 in Fig. 8c). In contrast to $Pd(C_2H_4)_2^{(\parallel)}$, the metal $3d_{yz}$- and ligand $(\pi_1^* + \pi_2^*)$-orbitals are already moderately correlated. Their correlation further increases when the ethene ligands approach the metal center (see Fig. 8b). Around the equilibrium structure, the strong correlation between the Ni $3d_{z^2}$- and $4s$-orbitals diminishes and the bonding and antibonding combination of the Ni $3d_{z^2}$-orbital and the ligand $(\pi_1 - \pi_2)$-orbital (nos. 3 and 6 in Fig. 8a) are strongly correlated. The latter orbital correlation corresponds to the metal-to-ligand π-donation mechanism. In contrast to the monoligated $Ni(C_2H_4)$ complex (see Ref. [16] for details), π-donation does not commence until close to the equilibrium geometry and the corresponding orbital correlations are comparable to those between the Ni $3d_{yz}$- and ligand $(\pi_1^* + \pi_2^*)$-orbitals.

The reaction pathway of $Ni(C_2H_4)_2^{(\perp)}$ features a notably different evolution of orbital correlation and entanglement compared to its structural isomer $Ni(C_2H_4)_2^{(\parallel)}$. In the vicinity of dissociation (Fig. 9c), the Ni $3d_{x^2-y^2}$- and $4d_{x^2-y^2}$-orbitals (nos. 4 and 7) as well as the ligand $(\pi_1, \pi_2)^*$- and (π_1^*, π_2^*)-orbitals (nos. 14, 22, and 30) are strongly correlated with each other, while the orbitals involved in metal-to-ligand back-bonding (nos. 21 and 22 as well as nos. 29 and 30) are moderately correlated. When the ethene ligands approach the metal center (Fig. 9b), metal and ligand orbitals that participate in π-donation (nos. 5 and 6) are weakly correlated, while those important for metal-to-ligand

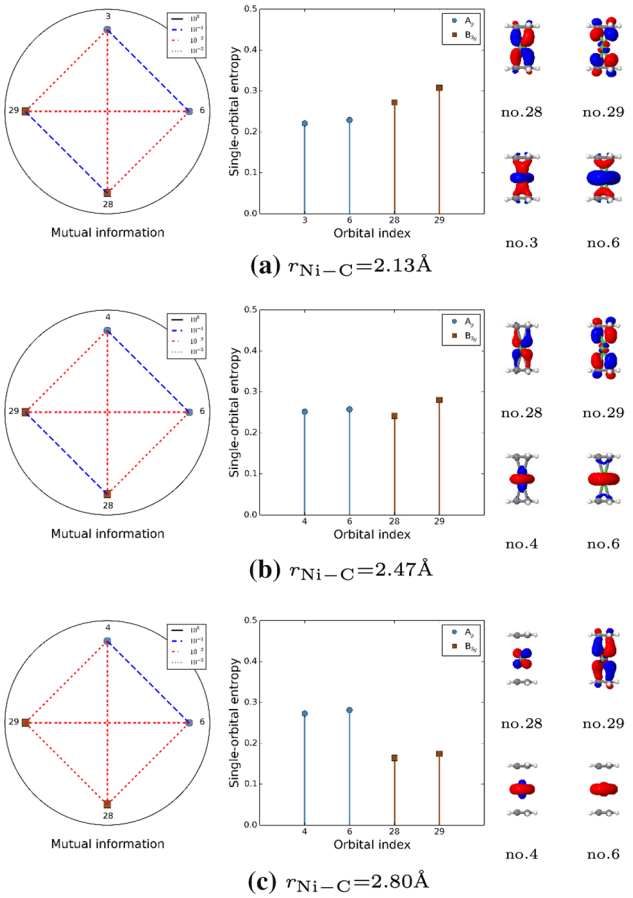

Fig. 8 Orbital-pair mutual information and single-orbital entropy for $Ni(C_2H_4)_2^{\parallel}$ determined from DMRG(34,33) calculations. Only the strongly correlated/entangled orbitals are shown, i.e., $s(1)_i > 0.1$ and $I_{i|j} > 10^{-2}$

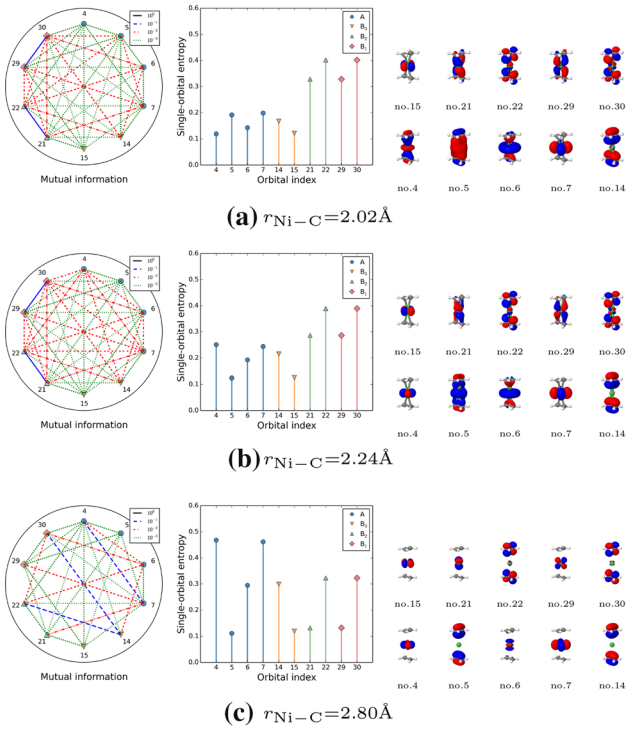

Fig. 9 Orbital-pair mutual information and single-orbital entropy for $Ni(C_2H_4)_2^{\perp}$ determined from DMRG(36,33) calculations. Only the strongly correlated/entangled orbitals are shown, i.e., $s(1)_i > 0.1$ and $I_{i|j} > 10^{-2}$

back-bonding (nos. 21 and 22 as well as nos. 29 and 30) are strongly correlated. Close to the equilibrium geometry (Fig. 9a), we observe a transition of orbital entanglement and correlation patters. Specifically, the correlation between the Ni 3*d*- and 4*d*-orbitals (nos. 4 and 7) decreases when approaching the equilibrium geometry. Similar to $Pd(C_2H_4)_2^{\perp}$, the orbital correlation and entanglement analysis suggest that $Ni(C_2H_4)_2^{(\perp)}$ features two metal-to-ligand back-bonding interactions, while the $Ni(C_2H_4)_2^{(\parallel)}$ isomer displays one strong metal-to-ligand back-bonding and π-donation interaction.

Comparison of the bonding mechanism in Ni- and Pd-olefines Finally, we will compare the bond-formation process and the bonding interactions in nickel–ethene and palladium–ethene complexes. Both the EDA and orbital entanglement analysis highlight the different nature of the metal–ethene bond and of the bond-formation mechanism. In general, the bonding interaction in the nickel–ethene complexes is stronger than in the corresponding palladium–ethene compounds. Furthermore, the degree of covalency of the metal–olefin bond is higher for nickel–ethene than for palladium–ethene [cf. the large values of ΔE_{oi} for $Ni(C_2H_4)_x$ compared to $Pd(C_2H_4)_x$ $(x = 1, 2)$]. The different bonding nature and bond-formation processes are supported by our orbital entanglement analysis. While the metal-to-ligand back-bonding mechanism plays an important role in the bond-formation process in nickel–olefin compounds and which establishes for stretched Ni−C_2H_4 distances in the vicinity of dissociation, the metal-to-ligand back-bonding in $Pd(C_2H_4)_x$ becomes important close to the equilibrium geometry. Similarly, the role of π-donation considerably differs in nickel–ethene and palladium–ethene. Specifically, our entanglement analysis predicts that the π-donation mechanism is insignificant in $Pd(C_2H_4)_x$ complexes, while it forms an essential part in the bond-formation process in $Ni(C_2H_4)_x$ compounds where the correlation between the ligand π-orbitals and the metal d_{z^2} -orbital increases when the ethene ligands approach the nickel center.

4 Conclusions

In this work, we investigated the interactions between ethene ligands and the nickel and palladium center along

the metal–ethene reaction coordinate and for perpendicular and parallel orientations of the ethene ligands. While both nickel and palladium are d^{10}-transition metals, they exhibit a considerably distinct bonding mechanism and interactions with ethene ligands. Specifically, nickel–carbon bonds are shorter and stronger than palladium–carbon bonds for both the parallel and perpendicular orientation. Moreover, the bond between nickel and ethene has predominantly covalent character, while the palladium–ethene bond has mainly ionic character.

Both d^{10}-transition metals create more stable complexes with ethene in perpendicular orientation, where two metal-to-ligand back-bonding mechanisms can be observed. The double-back-bonding allows for stronger orbital interactions. Moreover, our entanglement analysis indicates that molecular orbitals involved in π-donation from the ethene π-orbitals to the metal d_{z^2}-orbital are considerably more correlated in nickel–ethene than palladium–ethene complexes. Thus, while π-donation plays an important role in the bond-formation process of nickel–ethene, the palladium–ethene bond does not feature strong π-donation.

This work demonstrates that concepts from quantum information theory constitute a useful and complementary tool to well-established methods like energy decomposition analysis in dissecting chemical reactions.

Acknowledgments We gratefully acknowledge financial support from the Natural Sciences and Engineering Research Council of Canada (NSERC) and the Hungarian Research Fund (OTKA K100908 and NN110360). Y.Z. acknowledges financial support from the Mitacs Globalink program. K.B. acknowledges financial support from the Swiss National Science Foundation (P2EZP2 148650), the Banting Postdoctoral Fellowship program, and the National Science Center Poland, Grant No. DEC-2013/11/B/ST4/00771. P.T. gratefully acknowledges financial support from the National Science Center Poland, Grant No. DEC-2012/07/B/ST4/01347 and No. DEC-2013/11/B/ST4/00771. C.D. acknowledges financial support from the McMaster Chemistry & Chemical Biology Summer Research Scholarship and the NSERC Undergraduate Student Research Award fellowship. The authors acknowledge support for computational resources from SHARCNET, a partner consortium in the Compute Canada national HPC platform.

References

1. Milstein D, Stille JK (1979) J Am Chem Soc 101:4992
2. Denmark SE, Ober MH (2003) Aldrichim Acta 36:75
3. Zeni G, Larock RC (2004) Chem Rev 104:2285
4. Sindlinger CP, Weiß S, Schubert H, Wesemann L (2015) Angew Chem Int Ed 54:4086–4091
5. Nishimura A, Ohashi M, Ogoshi S (2012) J Am Chem Soc 134:15692
6. Trost BM, Bringley DA, Seng PS (2012) Org Lett 14:234
7. Dewar M (1951) Bull Soc Chim Fr 18:C71
8. Chatt J, Duncanson L (1953) J Chem Soc 1953:2939–2947
9. Tsuji J (1969) Acc Chem Res 2(5):144
10. Ozin GA, Power WJ (1977) Inorg Chem 16:212
11. Jarque C, Novaro O, Ruiz M (1987) Mol Phys 62:129
12. Blomberg MRA, Siegbahn PEM, Svensson M (1992) J Phys Chem 96(24):9794
13. Minaev B, Agren H (1998) Int J Quantum Chem 72:581
14. Rappé AK, Skiff WM, Casewit CJ (2000) Chem Rev 100(4):1435
15. Dedieu A (2000) Chem Rev 100(2):543
16. Duperrouzel C, Tecmer P, Boguslawski K, Barcza G, Legeza Ö, Ayers PW (2015) Chem Phys Lett 621:160
17. Bernardi F, Bottoni A, Calcinari M, Rossi I, Robb MA (1997) J Phys Chem A 101:6310
18. Kitaura K, Morokuma K (1976) Int J Quantum Chem 10:325
19. Umeyama H, Morokuma K, Yamabe S (1977) J Am Chem Soc 99:330
20. Ziegler T, Rauk A (1977) Theor Chim Acta 46:1
21. Ziegler T, Rauk A (1979) Inorg Chem 18:1558
22. Ziegler T, Rauk A (1979) Inorg Chem 18:1755
23. Bickelhaupt FM, Baerends EJ (2007) Kohn-Sham density functional theory: predicting and understanding chemistry, vol 15. Wiley, New York
24. Hopffgarten MV, Frenking G (2012) WIREs Comput Mol Sci 2(1):43
25. Wolters LP, Bickelhaupt FM (2013) ChemistryOpen 2:106
26. Wolters LP, Van Zeist WJ, Bickelhaupt FM (2014) Chem Eur J 20:11370
27. Boguslawski K, Tecmer P (2015) Int J Quantum Chem 115:1289. doi:10.1002/qua.24832
28. Szalay S, Pfeffer M, Murg V, Barcza G, Verstraete F, Schneider R, Legeza Ö (2015) Int J Quantum Chem 115:1342. doi:10.1002/qua.24898
29. Rissler J, Noack RM, White SR (2006) Chem Phys 323:519
30. Barcza G, Legeza Ö, Marti KH, Reiher M (2011) Phys Rev A 83:12508
31. Boguslawski K, Tecmer P, Legeza Ö, Reiher M (2012) Phys Chem Lett 3:3129
32. Boguslawski K, Tecmer P, Barcza G, Legeza Ö, Reiher M (2013) J Chem Theory Comput 9:2959
33. Legeza Ö, Sólyom J (2003) Phys Rev B 68:195116
34. Barcza G, Noack R, Sólyom J, Legeza Ö (2014) arXiv preprint arXiv:1406.6643
35. Legeza Ö, Sólyom J (2006) Phys Rev Lett 96:4
36. Tecmer P, Boguslawski K, Legeza Ö, Reiher M (2014) Phys Chem Chem Phys 16:719
37. Boguslawski K, Reiher M (2014) Chemical bonding in open-shell transition-metal complexes. In: Frenking G, Shaik S (eds) The chemical bond: chemical bonding across the periodic table. Wiley VCH Verlag GmbH & Co. KGaA, Weinheim
38. Mottet M, Tecmer P, Boguslawski K, Legeza Ö, Reiher M (2014) Phys Chem Chem Phys 16:8872
39. Freitag L, Knecht S, Keller SF, Delcey Pedersen MG, Aquilante F, Bondo T, Lindh R, Reiher M, Gonzalez L (2015) Phys Chem Chem Phys 17:13769
40. Tecmer P, Boguslawski K, Ayers P (2015) Phys Chem Chem Phys 17:14427
41. Fertitta E, Paulus B, Barcza G, Legeza Ö (2014) Phys Rev B 90:245129

42. Murg V, Verstraete F, Schneider R, Nagy PR, Legeza Ö (2015) J Chem Theory Comput 11(3):1027
43. te Velde G, Bickelhaupt FM, van Gisbergen SJA, Guerra CF, Baerends EJ, Snijders JG, Ziegler T (2001) J Comput Chem 22:931
44. Guerra CF, Snijders JG, te Velde G, Baerends EJ (1998) Theor Chim Acta 99:391
45. ADF2013.01, SCM, Theoretical Chemistry, Vrije Universiteit, Amsterdam, The Netherlands, http://www.scm.com
46. Lenthe EV, Baerends EJ, Snijders JG (1993) J Chem Phys 99:4597
47. van Lenthe E, Baerends EJ, Snijders JG (1994) J Chem Phys 101:9783
48. Van Lenthe E, Ehlers A, Baerends EJ (1999) J Chem Phys 110:8943
49. Van Lenthe E, Baerends EJ (2003) J Comput Chem 24:1142
50. Perdew JP (1986) Phys Rev B 33:8822
51. Becke A (1988) Phys Rev A 38:3098
52. Roos B, Taylor PR (1980) Chem Phys 48:157
53. Siegbahn PEM, Almlöf J, Heiberg A, Roos BO (1981) J Chem Phys 74:2384
54. Werner HJ, Knowles PJ (1985) J Chem Phys 82(11):5053
55. Aidas K, Angeli C, Bak KL, Bakken V, Bast R, Boman L, Christiansen O, Cimiraglia R, Coriani S, Dahle P et al (2013) WIREs Comput Mol Sci 4:269
56. Werner HJ, Knowles PJ, Knizia G, Manby FR, Schütz M (2012) WIREs Comput Mol Sci 2:242
57. Werner HJ, Knowles PJ, Lindh R, Manby FR, Schütz PCM, Korona T, Mitrushenkov A, Rauhut G, Adler TB, Amos RD, Bernhardsson A, BerningA, Cooper DL, Deegan MJO, Dobbyn AJ, Eckert F, Goll E, Hampel C, Hetzer G, Hrenar T, Knizia G, Köppl C, Liu Y, Lloyd AW, Mata RA, May AJ, McNicholas SJ, Meyer W, Mura ME, Nicklass A, Palmieri P, Pflüger K, Pitzer R, Reiher M, Schumann U, Stoll H, Stone AJ, Tarroni R, Thorsteinsson T, Wang M (2012) A Wolf Molpro, version2012.1, a package of *ab initio* programs. See http://www.molpro.net
58. Widmark PO, Malmqvist PA, Roos BO (1990) Theor Chim Acta 77:291
59. Roos BO, Lindh R, Malmqvist PA, Veryazov V, Widmark PO (2004) J Phys Chem A 108:2851
60. Roos BO, Lindh R, Malmqvist PA, Veryazov V, Widmark PO (2005) J Phys Chem A 109:6575
61. Douglas N, Kroll NM (1974) Ann Phys 82:89
62. Hess BA (1986) Phys Rev A 32:3742
63. Jmol: an open-source Java viewer for chemical structures in 3D. http://www.jmol.org/
64. Knowles PJ, Hampel C, Werner HJ (1993) J Chem Phys 99:5219
65. Legeza Ö. QC-DMRG-Budapest, a program for quantum chemical DMRG calculations. Copyright 2000–2013, HAS RISSPO Budapest
66. Peschel I, Want X, Kaulke M, Hallberg K (1999) In: Density-matrix renormalization, a new numerical method in physics, vol. 528
67. White SR (1992) Phys Rev Lett 69:2863
68. White SR (1993) Phys Rev B 48:10345
69. Bartlett RJ, Stanton JF (1994) Rev Comput Chem 5:65
70. Bartlett RJ, Musiał M (2007) Rev Mod Phys 79:291